The investigation of high intensity laser driven micro neutron sources for fusion materials research at high fluence

L.J. Perkins, B.G. Logan, M.D. Rosen, M.D. Perry, T. Diaz de la Rubia, N.M. Ghoniem*, T. Ditmire, P.T. Springer, S.C. Wilks

Lawrence Livermore National Laboratory,
Livermore, California

* University of California,
Los Angeles, California

United States of America

Abstract. The application of fast pulse, high intensity lasers to drive low cost DT point neutron sources for fusion materials testing at high flux/fluence is investigated. At present, high power bench-top lasers with intensities of 10^{18} W/cm^2 are routinely employed and systems capable of $\geq 10^{21}$ W/cm^2 are becoming available. These potentially offer sufficient energy density for efficient neutron production in DT targets with dimensions of around 100 μm. Two different target concepts are analysed — a hot ion, beam–target system and an exploding pusher target system — and neutron emission rates are evaluated as a function of laser and target conditions. Compared with conventional beam–target neutron sources with steady state liquid cooling, the driver energy here is removed by sacrificial vaporization of a small target spot. The resulting small source volumes offer the potential for a low cost, high flux source of 14 MeV neutrons at close coupled, micro ($\leq$1 mm) test specimens. In particular, it is shown that a laser driven target with $\sim$100 J/pulse at 100 Hz (i.e. $\sim$10 kW average power) and laser irradiances in the range $I\lambda^2 \sim 10^{17}$–10^{19} W μm^2/cm^2 could produce primary, uncollided neutron fluxes at the test specimen in the 10^{14}–10^{15} n cm^{-2} s^{-2} range. While focusing on the laser–plasma interaction physics and resulting neutron production, the materials science required to validate computational damage models utilizing $\geq$100 dpa irradiation of such specimens is also examined; this may provide a multiscale predictive capability for the behaviour of engineering scale components in fusion reactor applications.

1. Introduction

The last ten years or so have witnessed a rapid expansion in the field of short pulse, high intensity lasers [1, 2]. Pulse lengths have fallen from tens of picoseconds in the mid-1980s to state of the art $\sim$10 fs today. The ability to generate light pulses three orders of magnitude shorter means that, for the same energy and the same approximate cost, intensities have increased by the same factor. Thus today intensities of 10^{18} W/cm^2 are routinely available from bench-top lasers and systems capable of $\sim 10^{21}$ W/cm^2 are now starting to come on-line. In particular, access to high temperature states of matter capable of thermonuclear fusion and/or the efficient production of hot ions for beam–target fusion is now within reach using small scale, bench-top lasers.

In this paper, we investigate the prospects for utilizing such intense, bench-top scale laser systems to drive low cost, intense 14 MeV DT neutron sources with either fast-ion-driven micro-targets or exploding pusher targets. Such targets permit the close positioning of small ($\sim$1 mm) micro test specimens of fusion relevant materials (e.g., ferritic steel, vanadium alloy, carbon, silicon carbide) and the potential for obtaining neutron fluxes around 10^{15} n cm^{-2} s^{-1}. A complementary materials science and computational modelling programme could then validate damage models for materials lifetimes $\geq$100 dpa and provide a multiscale predictive capability for the extrapolated behaviour of engineering scale components. Such a coupled irradiation–computation programme might partially compensate for the absence of large scale testing with high fluence, volumetric fusion plasmas.

The irradiation environment of DT fusion reactors, both inertial and magnetic, consists of 14.1 MeV neutrons plus a large fraction ($\sim$80% at the first

wall surface) of lower energy, collided neutrons. For a neutron wall load, i.e. neutron power flux, at the first wall of, say, 5 MW m^{-2}, the primary, uncollided neutron current is 2.2×10^{14} n cm^{-2} s^{-1} and the total flux is in excess of 10^{15} n cm^{-2} s^{-1}. In magnetic fusion reactors with solid walls and inertial fusion reactors with thin wetted walls guided by solid or compliant structures, significant damage will be sustained. A number of specific reactions result from such neutron interactions including hydrogen and helium production, atomic displacements and transmutations [3, 4]. Detrimental consequences include changes in thermophysical and thermomechanical properties, swelling, embrittlement, creep and sintering. End of life damage limits are estimated to be around 100–200 dpa for candidate structural metals and in the range 10–50 dpa for non-metals such as ceramics and composites [3–5]. These correspond to primary neutron fluences, i.e. time integrated currents, of approximately 10–20 MW a/m^2 ($\approx(1.4-2.8) \times 10^{22}$ n cm^{-2}) and 1–5 MW a/m^2 ($\approx(1.4-7) \times 10^{21}$ n cm^{-2}), respectively. Thus damage due to neutrons is a crucial factor in determining design limits and predicted lifetimes for fusion structural and blanket materials. Of course, the cost of obtaining such materials damage data is an important issue, especially where 14 MeV DT neutrons are concerned. Minimizing the source volume is one way to reduce cost through significantly lower drive requirements and tritium inventories.

Point neutron sources offer an attractive option for materials irradiation testing because of their simplicity, easy access and relatively low cost. From the descriptions above, the desired characteristics of such sources are:

(a) Capability of producing high damage rates in the range 20–100 dpa/a, corresponding to primary, uncollided neutron currents of $\sim(1–4) \times 10^{14}$ n cm^{-2} s^{-1} (i.e. ~2–10 MW m^{-2} for DT neutrons).

(b) Small neutron source volume for low cost. A test specimen cannot be placed closer than a distance determined by the emitting volume plus the heat removal hardware.

(c) A neutron source energy which provides a damage spectrum similar to that of a DT fusion reactor; this implies that a 14 MeV DT neutron source is highly desirable.

(d) High availability over extended periods of time.

2. System overview

Figure 1 shows our concept of a laser driven neutron source. Laser energies of around 100–1000 J/pulse at repetition rates of ~10–100 Hz (i.e. average powers of ~10 kW) will be required to yield primary uncollided neutron currents $\geq 10^{14}-10^{15}$ n cm^{-2} s^{-1} at material specimens mounted with stand-off distances of the order of millimetres from the target midpoint. These parameters together with requirements for laser pulse duration, focal spot and irradiance $I\lambda^2$ will be discussed in detail. Neutron producing targets of a few tens of micrometres diameter are mounted ~1–10 cm apart on a continuous foil strip which moves each target into the firing position at speeds of ~0.1–10 m/s. Three target options have been studied and will be described below. A sacrificial foil debris shield moving with the targets protects the material test specimen matrix which is coupled as closely as running clearances permit, i.e. about $\leq$0.2 cm from the front face of the specimen to the centre of the neutron production volume. The material test specimens have typical dimensions of ~1 mm. As noted above, the first wall environment of a DT fusion reactor consists of an appreciable fraction of lower energy, backscattered neutrons together with the 14.1 MeV peak. The damage characteristics of the first wall and blanket materials are then a convolution over this composite spectrum. Accordingly, careful design of the neutron shield surrounding the target area shown in Fig. 1 together with its material zoning will be important to simulate the expected spectral conditions at a typical fusion reactor first wall.

A possible alternative to the continuous target strip is to inject the targets in a manner similar to that envisaged for inertial confinement fusion reactors [6]. However, this option would need careful attention to injection geometry and positioning jitter to minimize target–specimen stand-off distances, otherwise neutron fluxes at the specimen will be significantly reduced. Moreover, a fixed debris shield would be required, thus increasing source–specimen distances. In general, therefore, the feasibility of individual target injection appears questionable compared with the continuous strip approach.

In Table 1, we compare the main features of this laser driven scheme with other candidate neutron sources for fusion materials testing. Some, like the subject of this article, are in the conceptual stage while others have seen considerable prior use.

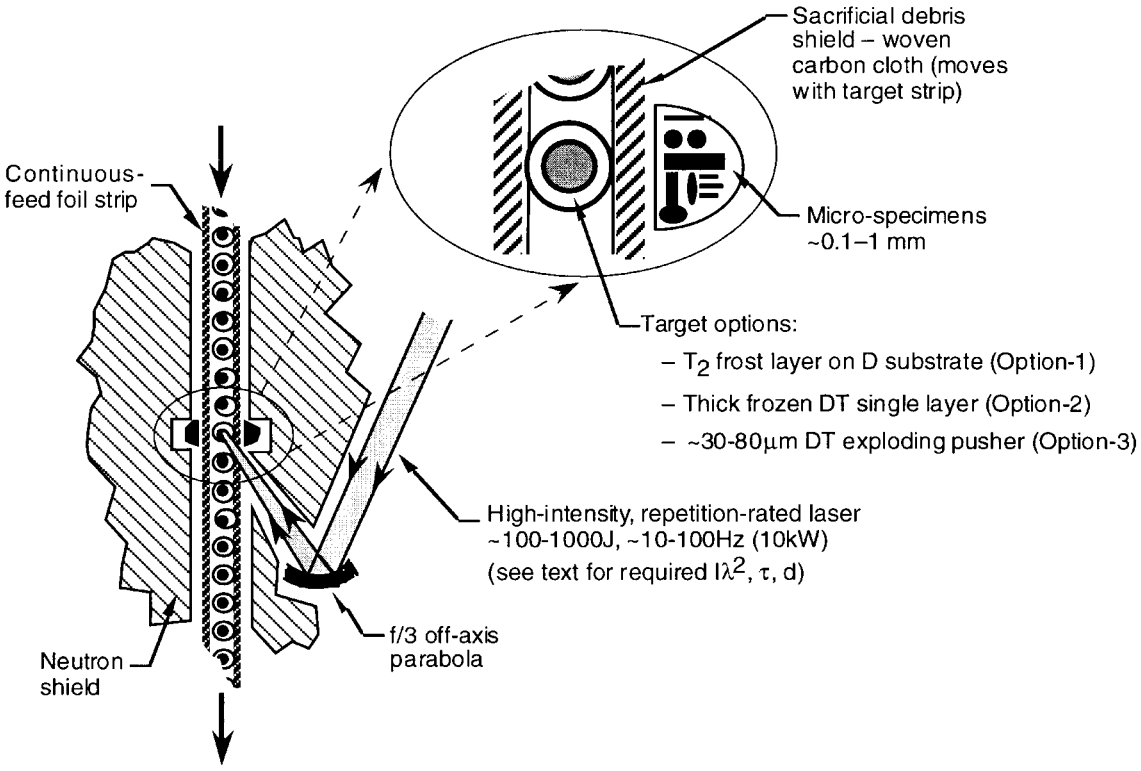

Figure 1. Schematic view of a micro-DT neutron source driven by a short pulse, high average power laser (not to scale). Target options 1–3 are described in Fig. 2.

Fission reactors are presently the workhorse for high flux testing of fusion materials. Unfortunately, the conditions in a fission reactor are not the same as those expected in a fusion reactor. Neutron energy spectra are different, with the consequence that the generated recoil spectrum in the materials is different [5]. Moreover, large quantities of helium and transmutation products will be produced in threshold (n, X) reactions in the fusion environment which are not present in fission reactors. We note also from Table 1 the possibility of employing existing or near term spallation neutron sources. However, it has been judged that spurious charged particle production due to the high energy tail of the neutron spectrum ($\gg 20$ MeV) and the low dpa generation rate make these of limited use to fusion materials research [7, 8].

In the absence of a test facility with a prototypical fusion spectrum, fission reactors will continue to remain the primary facilities for fusion materials irradiation. The value of fission reactors can be enhanced by innovative techniques to better simulate helium and hydrogen production through, for example, helium charging and boron or nickel doping. However, in a fusion reactor, the projected helium to dpa ratio is typically ∼4–15 appm/dpa for vanadium alloys and ferritic steels, and an order of magnitude higher in SiC and graphite. Deeper in the structure where the neutron spectrum is softer, these ratios drop because of their typically higher energy thresholds, and fission simulations become more relevant. But in the critical first few neutron mean free paths from the first wall, the primary damage state for microstructural and compositional changes is rather dissimilar for fission and fusion irradiation. An example is the helium production reactions in carbon bearing materials where the $^{12}\mathrm{C}(\mathrm{n}, \alpha)$ and $^{12}\mathrm{C}(\mathrm{n}, 3\alpha)$ reactions have thresholds of 6.2 and 8.3 MeV, respectively. A detailed discussion of candidate fusion neutron sources and their spectral differences can be found in Ref. [5]. References to the various concepts shown in Table 1 can be found in column 3 of the table.

It appears that no existing neutron source offers the necessary combination of neutron flux, spectrum and cost effectiveness. Relative to the other

Table 1. Classes of neutron sources for fusion material testing

	Description	Examples*	Neutronics specifications (typical)	Dimensions of emitting volume (typical)	Input power Facility cost Tritium useage	Comments
Laser based micro neutron sources	High intensity, laser driven; close coupled, microsamples	• Fast ion beam–target • Exploding pusher target (c)	$\sim\leq 10^{15}$ cm^{-2} s^{-1} over microsamples (1 mm). 14 MeV DT spectrum	~0.5–0.1 cm (fast ion range in substrate)	~10 kW. ≤US M$100 $\sim 3\times10^{-4}$ g/d	This article. Low cost, high fluxes, small testing volume (~1 cm^3), specimen sizes of ~1 mm.
Accelerator based, DT beam–target	~370 keV, ~150 mA deuterium beam; H_2O cooled T–Zr target	• RTNS-II (s) (Ref. [9])	$\sim 5\times10^{12}$ cm^{-2} s^{-1} over 1 cm^3 test volume. 14 MeV DT spectrum	~1 cm (beam spot diameter)	~50 kW. ~US M$25 $\sim 2\times10^{-5}$ g/d	Heat removal at large, water cooled solid target limits flux and fluence. Not relevant for high flux/fluence.
Accelerator based, D–Li beam–target	~30–40 MeV, ~250 mA deuterium beam on liquid lithium target	• IFMIF (c) (Ref. [10])	$\sim 9\times10^{13}$ (2.2×10^{14}) cm^{-2} s^{-1} over 500 (100) cm^3 test volumes. D–Li neutron spectrum	~10 cm (beam footprint)	~10 MW. ~US B$1 N/A	Neutrons from forward peaked, stripping reaction. Uncertainties in damage relevance due to $E_n \geq$ 20–40 MeV.
Spallation sources	800 MeV–GeV proton beam at ~10s mA on water cooled tungsten	• LANSCE (o) • IPNS (c) (Ref. [11])	$\leq 10^{13}$ cm^{-2} s^{-1} over $\sim 20\times10^3$ cm^3 test volumes. Spallation neutron spectrum.	~10s cm to metres (proton range)	~10s MW. ~US B$ for new facilities. N/A	Significant uncertainties in damage relevance due to spallation spectral components ($E_n \gg$ 20 MeV)
Fusion based high flux sources	Neutral beam heated 200 eV mirror plasma. 0.17–1 MW fusion power	• BPNS (c) • GDT (c) (Refs [12, 13])	$\geq 4(1)\times10^{14}$ cm^{-2} s^{-1} over 600 cm^3; $\geq 10^{13}$ over 0.6 (0.04) m^3 14 MeV DT spectrum	~20(10) cm (neutral beam range in target plasma	60(13) MW ~US B$1(0.5) ~0.9 g/d	Most fusion relevant. Medium test volumes. Dependent on international fusion development strategy.
Fusion reactor volumetric sources	High average power MFE or IFE test facilities. Typically driven at moderate Q	• VNS (MFE) (c) • ETF (IFE) (c) (Ref. [14])	$\sim 4\times10^{13}$–2×10^{14} cm^{-2} s^{-1} Large volumes (~m^3). 14 MeV DT spectrum	~2 m (plasma minor diameter)	~100s MW. ~US B$3–5 ~8 g/d	Most fusion relevant. Large test volumes. Significant cost. dependent on international fusion development strategy.
Fission reactors	In-core specimens in existing fission reactors	• HFIR (o) • HFBR (o/s) • ATR (o) (Ref. [15])	10^{14} – 2×10^{15} cm^{-2} s^{-1}, 10s cm^3 volumes. Fission neutron spectrum	~1 m (core diameter)	~100s MW ~US B$s for new facilities. N/A	Thermal or mixed fission spectrum; not very fusion relevant. High flux. Available facilities will decline in future years.

* (o) = operating. (s) = shut down. (c) = conceptual design. RTNS-II = Rotating Target Neutron Source (LLNL); IFMIF = International Fusion Materials Irradiation Facility; BPNS = Beam plasma neutron source; GDT = Gas dynamic trap; VNS = Volumetric neutron source (spherical tokamak); ETF = IFE Engineering Test Facility; HFIR = High Flux Irradiation Reactor (ORNL); ATR = Advanced Test Reactor (Naval, INEL); HFBR = High Flux Beam Reactor (BNL); SNS = Intense Pulsed Neutron Source (ORNL); LANSCE = Los Alamos Neutron Science Center [5, 9–15].

candidates in Table 1 and, in particular, to the other beam–target sources, the laser driven concepts of this article may offer the following advantages:

(a) Very small target volumes due to high laser intensities and laser heat removal by sacrificial vaporization rather than by the steady state, liquid cooling methods of conventional beam–target neutron sources (see, e.g., Refs [9, 10]). This provides the opportunity to close-couple irradiation specimens resulting in very high point neutron fluxes at low power and low cost.

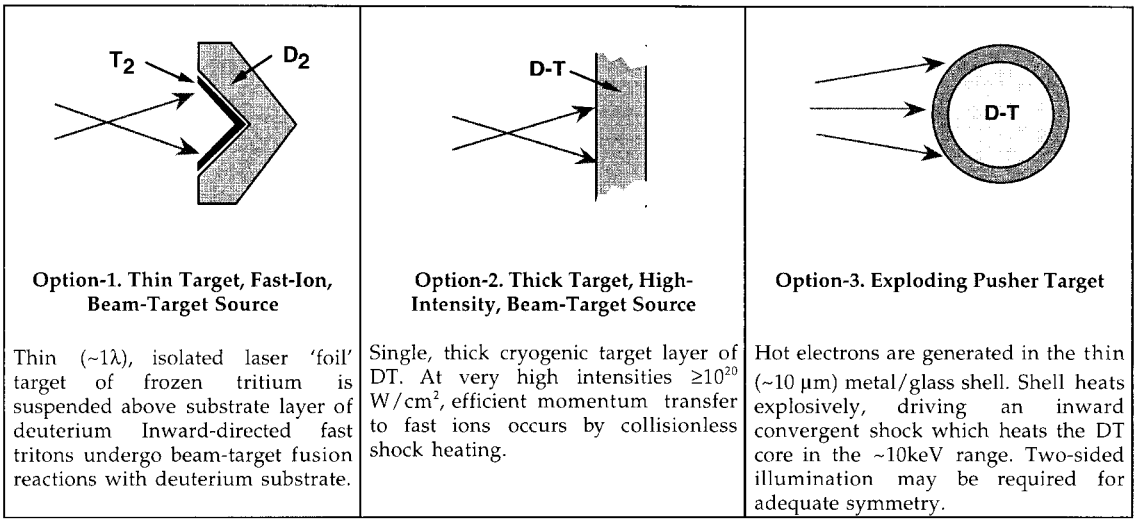

Option-1. Thin Target, Fast-Ion, Beam-Target Source	Option-2. Thick Target, High-Intensity, Beam-Target Source	Option-3. Exploding Pusher Target
Thin (~1λ), isolated laser 'foil' target of frozen tritium is suspended above substrate layer of deuterium Inward-directed fast tritons undergo beam-target fusion reactions with deuterium substrate.	Single, thick cryogenic target layer of DT. At very high intensities $\geq 10^{20}$ W/cm^2, efficient momentum transfer to fast ions occurs by collisionless shock heating.	Hot electrons are generated in the thin (~10 μm) metal/glass shell. Shell heats explosively, driving an inward convergent shock which heats the DT core in the ~10keV range. Two-sided illumination may be required for adequate symmetry.

Figure 2. The three target options.

(b) The prospects for self-heated plasma targets. In the case of the fast ion beam–target schemes described below, this provides significantly higher neutron production rates per incident watt relative to conventional, beam–target neutron sources with cold (i.e. solid or liquid) targets.

(c) Low cost. The cost of fast pulse, intense lasers scales approximately as the energy per pulse, with pulse length and repetition rate only a secondary cost issue up to some heat removal limit. Thus, the average power of the system and, therefore, the time averaged neutron flux, is ultimately determined by the heat removal limitations in the laser.

(d) The production of a pure DT neutron spectrum. This provides for fusion material irradiation experiments that are free of the spectral uncertainties accompanying irradiations in fission reactors [15], spallation sources [9] and D–Li accelerators [5, 10].

Note from Table 1 that the cost of the various irradiation facilities tends to scale as the total fusion (or fission) power. By contrast, the maximum neutron flux attainable at material test specimens depends on the intensity of the source emitting volume and the minimum source sample stand-off distance. A laser driven neutron source potentially offers high neutron fluxes at modest cost. Of course, the small source volumes and close coupling means that the useful testing volume in the high flux zone is only of the order of 0.5 cm^3. Ultimately, of course, fusion energy development will require tests of heterogeneous fusion components, necessitating the use of large volume (and expensive) volumetric neutron sources. However, as discussed below, we suggest that the small dimensions of the material test specimens envisaged for use here (∼1 mm) do not present any fundamental difficulty regarding damage characterization of irradiated volumes of single materials and composites.

3. Laser target options

As shown in Fig. 2, we have studied three potential target concepts:

3.1. Option 1: thin target, fast ion, beam–target sources

A thin (∼ few micrometres) isolated laser 'foil' target of frozen tritium is suspended a few micrometres above a thicker substrate layer of deuterium. Laser energy absorbed by hot electrons electrostatically couples to ions in the foil resulting in the efficient production of fast tritium ions in the range of hundreds of keV. Isolation of the tritium layer is necessary to prevent the formation of a cold electron return current which otherwise would short out the ambipolar accelerating field (Section 4). The inward directed tritons undergo beam–target fusion reactions with the deuterium substrate. Fast ion heating raises the substrate's electron temperature in the range of hundreds of eV, thus reducing the ion stopping power for subsequent ions and significantly enhancing the neutron production rate per laser energy pulse. As discussed below, this scheme

is applicable to laser irradiances in the approximate range $I\lambda^2 \sim 10^{16}$–10^{18} W μm^2/cm^2, otherwise the fast ions are too slow or too energetic, respectively. Most of the analysis in this article will be devoted to this type of target.

3.2. Option 2: thick target, high intensity driven, beam–target sources

At higher laser irradiances $I\lambda^2 \geq 10^{18}$ W μm^2/cm^2, plasma electrons are driven relativistically. Hole boring of the laser light yields electron driven acceleration gradients producing energetic ions. At very high irradiances $\geq 10^{20}$ W μm^2/cm^2, efficient energy transfer to fast ions can occur by collisionless shock heating. Here, direct momentum transfer from the laser light to the ions drive the latter into the target. Unlike the analogous scheme in option 1 above, this produces fast ions directly for beam–target fusion without the need for the thin target layer isolated from the substrate. In this case, a single continuous cryogenic target layer of 50:50 DT might be employed of thickness equal to the optimum ion range, thus considerably simplifying target fabrication but at the expense of higher laser intensities in the range 10^{18}–10^{20} W μm^2/cm^2 and higher tritium inventories. Other considerations of the beam–target neutron production will be similar to those discussed below in connection with the analysis for option 1.

3.3. Option 3: exploding pusher target source

Hot electrons from a high intensity laser strike the outside of a thin ($\sim$ few micrometres) metal or glass shell enclosing a cryogenic solid or liquid DT core of $\sim$tens of micrometres radius. The shell heats rapidly to $\sim$keV temperatures, exploding the shell with many gigabar pressures and driving an inward shock at $\sim$several 10^7 cm/s. The convergent shock from the shell heats the DT core, yielding ion temperatures in the $\geq$10 keV range. Fuel burnup and the resulting neutron yield are determined by the dynamics of capsule disassembly. As discussed further in Section 6, because the DT fuel is preheated, it is on a high isentrope so the fuel radius converges by only a factor of $\sim$3. Thus, unlike conventional hot spot ICF targets, these 'exploding pusher' capsules do not scale to high gain. In the schematic diagram of Fig. 2, we show only single sided illumination of the capsule. However, adequate compression symmetry may require multi-sided illumination.

3.4. Other target options — atomic clusters

We also note that irradiation of noble-gas clusters ($\sim$1000s atoms/cluster) with high intensity laser pulses have produced highly ionized, very high temperature microplasmas [16, 17]. The explosion of these microclusters ejects ions with high kinetic energies. Beam–target neutrons could be produced from such fast ions in a manner analogous to the thin target, hot ion concept in option 1 above but with rather different target geometries. In particular, Ditmire has shown that in such clusters the efficiency of absorption of laser energy into fast ions can be in excess of 80% for laser intensities of $\sim 10^{16}$ W/cm^2 [17]. The mean fast ion energy here was $\sim$45 keV. Although the mechanism for such efficient hot ion production is not clear, it may be that the clusters are undergoing 'Coulomb explosions' where the electrons are completely removed leaving the ions to accelerate radially outwards under an electric field which scales as the square of the original cluster radius. We are currently examining the characteristics of such neutron sources, either as bare thermonuclear DT clusters or tritium clusters surrounded by a neutron producing, beam–target deuterium 'collar'. This will be reported in a future communication.

4. Laser interaction physics and requirements for efficient neutron production

A review of the literature on high intensity lasers from the past decade or so indicates that it is convenient to separate the interaction physics for a laser driven neutron source into three different irradiance regimes:

4.1. Irradiances $I\lambda^2 < 10^{17}$ W μm^2/cm^2

At lower intensities, $I\lambda^2 < 10^{17}$ W m^2/cm^2, the interaction of laser light occurs by inverse bremsstrahlung and collisional absorption [18]. For the target of option 1 operating in this regime, laser energy is initially absorbed entirely by plasma electrons. However, in the thin, isolated target layer, the space charge field of the heated electrons accelerates ions into the blow-off plasma and the frost layer explodes (see, e.g., Ref. [19]), resulting in significant fast ion production. In thicker single region targets at these lower intensities, we would expect that electron heat conduction into the target coupled with

the neutralizing effect of the cold returning electron current would result in little hot ion production.

From a review of experiments in the range $I\lambda^2 \sim 10^{11}$–10^{17} W μm^2/cm^2, Gitomer et al. [20] suggest a hot electron scaling of the following form:

$$T_{e,hot}\ (\text{keV}) \sim 1.6 \times 10^{-6}\ [I\lambda^2\ (\text{W}\ \mu\text{m}^2/\text{cm}^2)]^{4/9}. \tag{1}$$

They apply three analytic models to deduce the mean fast ion energy as

$$\bar{E}\ (\text{keV/amu}) \sim k_1 T_{e,hot}\ (\text{keV}) \tag{2}$$

with k_1 from the models being in the range $2/3^{1/2}$–12.5. Experimental data in the range $I\lambda^2 \leq 10^{17}$ W μm^2/cm^2 appear to be well fitted by $k_1 \sim 4$–5.

This scaling for fast ion energy is in agreement with the fact that the ion rich plasma resulting from expelled electrons should exhibit a sheath potential of [21]

$$V_{sheath} \sim \frac{kT_{e,hot}}{2e} \ln\left(\frac{m_i}{2\pi m_e}\right). \tag{3}$$

Similar scalings from Kruer and Estabrook [22, 23], Manes et al. [24] and Kruer [25] suggest

$$T_{e,hot}\ (\text{keV}) \sim k_2 [I\lambda^2\ (\text{W}\ \mu\text{m}^2/\text{cm}^2)]^{0.33} \tag{4}$$

where k_2 is in the range 6×10^{-5}–1.2×10^{-4}.

Fews et al. [26] have presented recent experimental evidence for such ion energies of ~0.2–1.3 MeV for intensities of $I = 2 \times 10^{17}$–2×10^{18} W/cm^2. Also, as noted above, Ditmire et al. have measured the absorption efficiency of laser energy into fast ions with peak laser intensities of 2×10^{16} W/cm^2 incident on clusters (~1000s atoms/cluster) [16, 17]. They find mean fast ion energies of ~45 keV and absorption efficiencies of 80–90%.

4.2. Irradiances $I\lambda^2 \sim 10^{18}$ W μm^2/cm^2

Collisional absorption becomes ineffective at irradiances of $I\lambda^2 \geq 10^{17}$ W μm^2/cm^2 because the plasma temperature rises too quickly for collisions to be effective (note that the electron–ion collision frequency goes as $\nu_{ei} \sim n/T_e^{3/2}$). In addition, at 10^{18} W μm^2/cm^2 the electron quiver velocity becomes comparable to the thermal velocity. In particular, the electron quiver energy E_{osc} (i.e. the cycle averaged, oscillatory energy of the electron in the laser field) is ~100 keV at 10^{18} W μm^2/cm^2 [1] requiring a relativistic treatment of the interaction process. This can result in relativistic self-focusing and channel formation leading to laser 'hole boring'. The hot electron energy can be several times E_{osc} and fast ions can then be accelerated through this ~MeV electron induced channel.

The hot electron temperature also depends on the polarization of the laser field, with p polarization, i.e. polarization in the plane of propagation, exhibiting a 2–3 times higher hot electron temperature than s polarization at the same laser intensity [27, 28]. Wilkes et al. [27] have performed particle in cell (PIC) simulations at irradiances of 10^{18}–10^{19} W μm^2/cm^2. At 10^{19} W μm^2/cm^2 they determined $T_e \sim 1.4$ MeV for p polarized light and also found fast ion energies of $\sim 10^{-3} m_0 c^2$ at the same intensity which translates to ~2 MeV for deuterons. Guethlein [29] has measured hot ion energies in excess of 1 MeV for laser intensities of $(2$–$3) \times 10^{19}$ W/cm^2 incident on aluminium and plastic targets.

Pretzler et al. [30] have observed DD neutron production through this proposed mechanism in deuterated polythene, using a 160 fs, 200 mJ laser with a 4.5 μm focal spot (implying $I \sim 10^{18}$ W/cm^2). Two effects are suggested to contribute to the channel formation. First, the relativistic mass increase of the quiver electrons in the focal region causes an increase in the refractive index and forms an effective positive lens. Second, as the sub-MeV electrons are accelerated forward, they generate megagauss fields leading to self-pinching of both the electrons and the light. Note that, in any event, the light pressure itself exceeds the plasma pressure. The result is a single narrow light propagation channel with diameter of several wavelengths and elongated over many Rayleigh lengths: i.e. the length for $1/e$ diffraction expansion. Not surprisingly, this regime is not well modelled by classical Spitzer–Harm conductivity.

Norres et al. [31] have observed similar beam–target DD neutron production with 1.3 ps, 1.05 μm light on flat targets of 120 μm thick deuterated polystyrene (C_8D_8) and also cryogenic deuterium pellets 0.5 cm thick. They ran with energies of ~8–20 J and average intensities of $\sim 8 \times 10^{18}$ W/cm^2. Their quoted DD yields of 7×10^7 neutrons/sr would result in a fusion Q value (fusion energy divided by laser input energy) of ~2% if operated in DT. As shown later, this implies both an efficient

transfer of laser energy into fast ion energy and beam–target interactions within a high temperature plasma background

4.3. Irradiances $I\lambda^2 \geq 10^{20}$ W μm^2/cm^2

At these very high intensities, the light pressure, $P = 2I/c \sim 600I$ (W/cm^2)/10^{18} Mbar, vastly exceeds the plasma pressure and momentum conversion from the ponderomotive force of the laser can occur directly to fast ions with high efficiency. Under such conditions, the properties of the plasma so produced are determined by the laser field rather than by its hydrodynamics. Note that, at $I = 10^{20}$ W/cm^2, the light pressure is $\sim 6 \times 10^4$ Mbar. The resulting collisionless shock can compress ion densities to several times that of the original preformed plasma [32]. Also, there are significant differences in the electron interaction physics relative to that occurring at lower intensities. First, because of the very short pulse duration, there is insufficient time for a substantial region of coronal plasma to form in front of the target. That is, the hydrodynamic timescale is longer than the pulse length. Second, because of the steep density gradients and hole boring, the laser energy is deposited at much higher electron densities than the critical density, which would otherwise limit long pulse penetration.

In this high intensity limit, momentum conservation yields ion velocities of

$$V_{ion} = 2(I/\rho c)^{1/2} \quad (5)$$

implying that the mean fast ion energy should scale as $\sim I$ rather than the $\sim I^{\sim 0.3-0.5}$ at lower intensities. Thus, at 10^{20} W/cm^2 in a deuterium target, this direct process should yield deuterons with energies approaching an MeV or so.

Denavit [32] has performed PIC simulations of interactions at $I = 10^{20}$–10^{21} W/cm^2 in thin, solid targets, demonstrating light transmission through plasmas which are overdense by factors of 10^2–10^3. Similarly, Lawson et al. [33] have modelled intensities in the range $I = 10^{18}$–10^{22} W/cm^2 in thin foils of aluminium and CH plastic. They find ions in the range of several hundred keV at $I = 10^{20}$ W/cm^2, consistent with Eq. (5) above, and $\sim$25% energy absorption efficiency into ions at $I = 10^{21}$ W/cm^2. Note, however, that both the results of Denavit and Lawson et al. apply to thin targets ($\ll 1\lambda$), which presumably will be influenced by electron space charge production.

4.4. Implications for efficient neutron production

From the evidence above, it appears that fast ion energies around 100–1000 keV are attainable in thin targets for laser irradiances of $\sim 10^{17}$ W μm^2/cm^2 due to acceleration by the space charge limited electron field and, interestingly, energies of the same order may be attainable for $I\lambda^2 \sim 10^{18}$ W μm^2/cm^2 to $I\lambda > 10^{20}$ W μm^2/cm^2 in thick targets due to relativistic hole boring and/or direct momentum transfer from the laser field. Moreover, energy conversion efficiencies into ions of $\sim$tens of per cent may be available throughout this range [16, 17, 20, 27, 32–34]. In general, scaling of hot ion energies and efficiencies tend as I^x, where $x \sim 0.3$–0.5 in the lower intensity regime and $x \sim 1$ in the high intensity regime.

To date there is no single model which can accommodate all the features of the interaction physics. Nor can present models adequately describe the transitions from lower to higher intensities, especially the effects of relativistic hole boring, the electron transport in the resulting high magnetic fields which persist on the hydrodynamic timescale, and the resulting energy coupling to ions. This situation calls for quantitative experiments. In particular, experiments are needed to determine the laser conditions at high intensity that might allow us to dispense with the thin, multilayer target geometry of option 1 above and employ the simpler single, thick target idea of option 2.

Thus, in the case of these beam–target schemes, an efficient, high-Q neutron source will require attention to the following:

(a) Efficient coupling of laser energy to hot electrons in the target.

(b) Efficient coupling of electron energy into fast ions or, at very high intensities, the efficient production of fast ions directly by the laser field.

(c) Production of fast ions in the energy range of several hundred keV to optimize DT neutron yield per unit laser energy dissipated in the target. Higher ion energies in the MeV range result in lower fusion Q values and have a long range in the target substrate, thus increasing the target–sample stand-off distance (Section 5).

(d) Concurrent heating of the target substrate to $\geq$100 eV to decrease the fast ion atomic stopping power and enhance the neutron yield per unit energy deposited in the target.

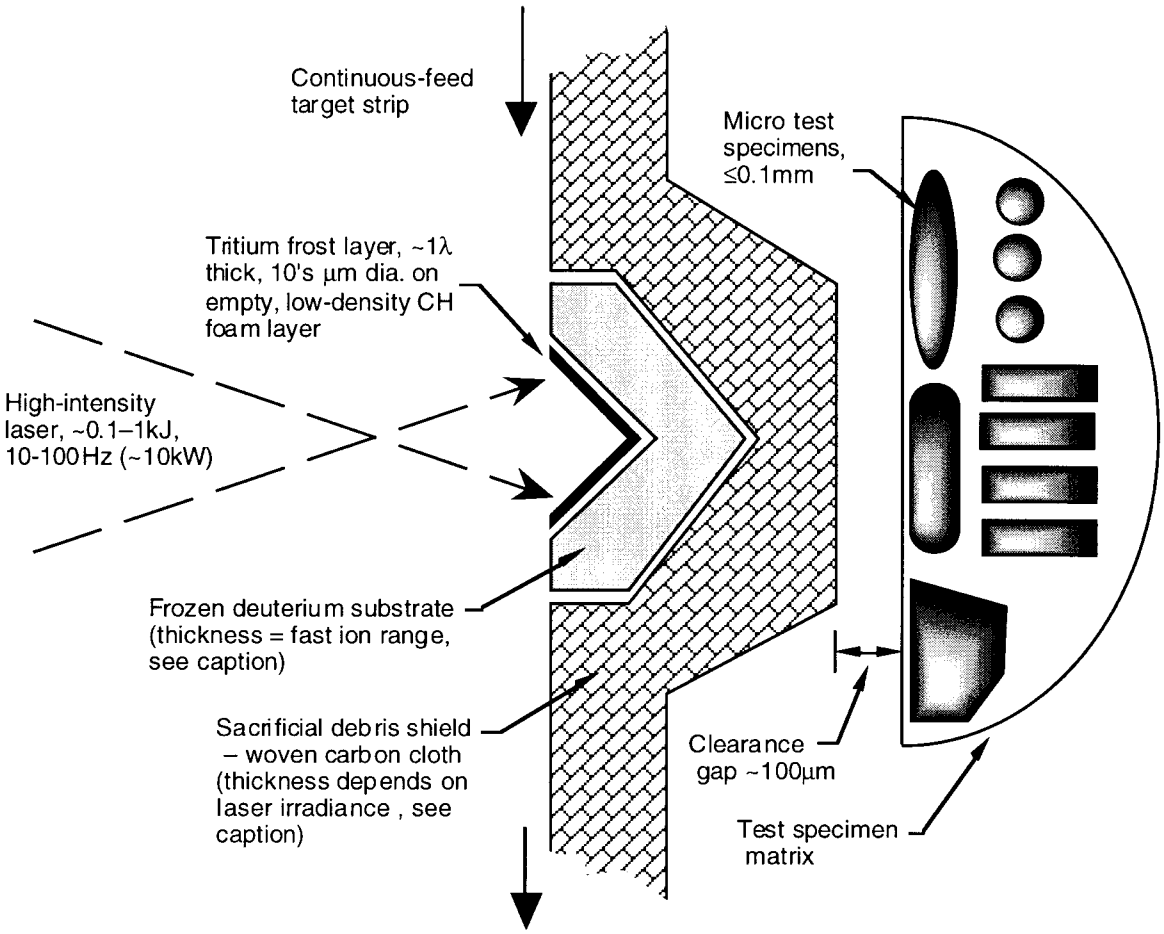

Figure 3. Schematic diagram of the target interaction region for option 1 (not to scale). The thickness of the deuterium substrate and debris shield are determined by the laser irradiance and resulting fast ion range and are described in Section 7. At high irradiances of $I\lambda^2 > 10^{18}$ W μm^2/cm^2, the multilayer thin target system here might be replaceable by a thick single region DT target.

5. Analysis for target option 1: thin target, hot ion, beam–target neutron sources

Figure 3 shows a schematic diagram of the target area for option 1. A thin (a few micrometres) layer of tritium frost is suspended above a frozen deuterium substrate of thickness tens to hundreds of micrometres depending on the fast ion energy and substrate electron temperature. Laser energy is absorbed by electrons in the tritium layer which become space charged limited as they stream from the interaction region. The ambipolar potential so formed electrostatically couples to the ions, and fast tritons are pulled explosively out of the target layer and enter the deuterium substrate. The thickness of the tritium film and its stand-off from the substrate must be maintained of the order of the electron sheath potential (i.e., a few micrometres), otherwise an internal cold electron return current will result, neutralizing the accelerating field. Depending on laser and target conditions an appreciable fraction of the incident laser energy can be converted to hot ions with energies in the range of hundreds of keV to ~1 MeV. The re-entrant conical target assembly is employed to enhance the inward direct ion current. The tritium frost layer can be suspended by deposition on to a low density foam which serves to separate the film from the substrate. Alternatively, we could consider a substrate of either a low density foam filled with cryogenic D_2 or a frozen CD_4 layer. Based on experimental observations, lasers of these intensities tend to punch clean holes into the targets, thus the

debris jet for the target shown in Fig. 3 would be forward peaked. In that respect, the debris shield would be increased in the rear direction and/or the specimen matrix would only be mounted in an approximate 250–300° arc around the target leaving the laser entrance and debris exit regions clear. Maintenance periods will be required to clean the target area ($\sim$ a few cm^3) of accumulated debris, preferably with a frequency no shorter than a day.

Tritium ions slowing down in the deuterium substrate give rise to 14 MeV fusion neutrons via T(d,n)^{4}He beam–target interactions. Concurrent ion and electron heating of the substrate decreases the ion stopping power resulting in longer ion ranges and significantly enhanced neutron production rates, as the following analysis will demonstrate.

At lower laser intensities $\leq 10^{17}$ W/cm^2, this process will only be efficient if the thin tritium layer is isolated from the deuterium substrate by a vacuum gap or a low density insulating foam as shown Fig. 3. In this way, the hot electrons are prevented from thermalizing in the substrate. Otherwise, a cold electron return current would occur, neutralizing the space charge field accelerating the fast ions. At high intensities $\geq 10^{18}$ W/cm^2, the single region thick target of option 2 may also yield an efficient hot ion current.

As illustrated in Fig. 1 above, targets are mounted 1–10 cm apart on a continuous plastic strip moving at about 0.1–10 m/s. We show below that laser energies of around 100–1000 J/pulse at repetition rates of $\sim$10–100 Hz (i.e. average powers of $\sim$10 kW) will be required to yield neutron fluxes $\geq 10^{14}$ n cm^{-2} s^{-1} at material specimens mounted with stand-off distances of $\sim$ millimetres from the target midpoint. A sacrificial shield of woven carbon cloth is sized (see below) to accommodate the laser blast and moves with the target strip to protect the material specimen from target debris. On the basis of our experimental observations, the laser should punch a clean precise hole though the strip and the debris jet will be strongly forward peaked. Maintenance periods will, however, be required to clean the $\sim$ few cm^3 target area of accumulated debris, preferably with a frequency no shorter than a few days.

An alternative option is to exchange the tritium and deuterium regions so that the laser interacts in a thin deuterium layer and the resulting fast deuterium ions stream into a tritium substrate. While this produces higher neutron fluxes at lower ion energies because of the greater energy available in the centre of mass for the DT cross-section (see below), it will also result in significantly larger tritium inventories. For the target option shown in Fig. 3, each target contains only about 4 μCi of tritium

To assess potential neutron yields and fluxes attainable with a candidate system, we introduce a 1-D slab model for laser interaction, ion slowing down and neutron production. Laser interaction with the thin, isolated tritium frost layer produces hot electrons of temperature $T_{e,hot}$ which electrostatically couple to fast tritons yielding an initial mean fast ion energy $\bar{E}_0$ incident on the deuterium substrate. As ions enter the substrate, they will begin to slow down, transferring energy to the medium by ionization, excitation and drag. Concurrently, the temperature of the substrate will begin to rise due to this ion deposition, supplemented by the fraction of laser produced hot electrons not contributing to the space charge limited ion production. The total energy lost by an ion with local energy E_{ion} traversing a distance x in the substrate is

$$\Delta E(E_{ion}, T) = \int_0^x \frac{dE}{dx}(E_{ion},\, T)dx \qquad (6)$$

where $dE(E_{ion}, T)/dx$ is the ion stopping power at substrate temperature T.

We assume the ion beam undergoes no angle scatter as it slows down (a good assumption until the end of the range where neutron production is anyway negligible). Also, as we are always in the limit that the nuclear reaction cross-section is small relative to the atomic slowing down cross-sections, we can neglect ion removal from the beam. Therefore, for an ion beam of cross-sectional area a_{ion} and flux φ_{ion} ions cm^{-2} s^{-1}, the neutron production rate from a slowing down element dx of volume $A_{ion}dx$ at depth x into the substrate is $n(x)\sigma(E_{ion}(x))\varphi_{ion}a_{ion}dx$, where σ is the DT cross-section at the local ion energy E_{ion} at depth x in the substrate and n is the local deuterium number density. Effecting a change of variable to the ion energy yields a total neutron yield (in units of n/s) of

$$Y(\bar{E}_0, T) = nJ(E_l, I\lambda^2) \int_{\bar{E}_0}^0 \frac{\sigma(E_{ion})dE_{ion}}{dE/dx(E_{ion}, T)} \qquad (7)$$

where $\bar{E}_0$ is the initial mean kinetic energy of the ion beam entering the substrate and $J(E_l, I\lambda^2) = a_{ion}\varphi_{\iota ov}$ is the fast ion current in ions/s, a function of the laser energy E_l and irradiance $I\lambda^2$. We also assume the deuterium density n is independent of depth in the target.

The resonance in the DT cross-section $\hat{\sigma}$ occurs at $\sim$64 keV in the centre of mass frame [35]. In the

laboratory frame, this translates to ∼160 keV for tritons incident on a deuterium target, or ∼107 keV for deuterons incident on a tritium target. However, because of the competition of atomic slowing down, ion energies somewhat above this peak are required to maximize the neutron yield in a thick beam–target system. The atomic cross-sections due to drag and ionization, which contribute to the ion stopping power dE/dx, are significantly larger than the nuclear interaction cross-section. Thus, in a cold target, the vast majority of ions slow down and stop in the target without producing a DT fusion reaction. Consequently, an ion starting out at high energy well above the peak in the fusion cross-section has a greater chance of producing a fusion neutron before its energy is reduced than an ion produced in the vicinity of the peak. Of interest here, a hot target with electron temperatures of tens to hundreds of eV has a significantly reduced dE/dx, thus enhancing the neutron yield for any ion birth energy. In general, the ion slowing down and resulting electron heating of the substrate occur in a time much less than the substrate disassembly time. Thus the substrate flashes to a high temperature solid plasma (Section 7). Of course, hotter targets exhibit lower values of dE/dx which result in higher neutron yields but also longer ion ranges and thus longer target–specimen stand-offs. Attention must be given, therefore, to both total yield and the neutron flux attainable at the specimen.

Formalisms for ion energy deposition in matter at finite temperatures have been developed by Mehlhorn [36], where the stopping power can be generalized to

$$\frac{dE}{dx}(E_{ion},T) = \left(\frac{dE}{dx}\right)_{bound} + \left(\frac{dE}{dx}\right)_{nuc} + \left(\frac{dE}{dx}\right)_{free} + \left(\frac{dE}{dx}\right)_{ion} \qquad (8)$$

and is a function of the average charge state $\bar{Z}_1$ of the projectile ion of atomic number Z_1 and the degree of ionization of the substrate z_{eff} of atomic number Z_2. The first term on the RHS of Eq. (8) accounts for energy loss due to ionization and excitation of bound electrons and is modelled by the Bethe equation [37] or, at low energies, by the Linhard–Scharff–Schiott model [38]. Shell corrections were applied by Mehlhorn to both models. The second term on the RHS of Eq. (8) represents elastic scattering between the ion and target nuclei of the substrate; it is only applicable at very low energies and particularly for large Z_1 and Z_2. As the ion beam heats the substrate, the resulting ionization increases the number of free electrons which can participate in the slowing down process and reduces the number of bound electrons. The third and fourth terms on the RHS of Eq. (8) account for the stopping power of these free electrons and of the resulting plasma ions, respectively. The ion term only becomes appreciable at high plasma temperatures where the ion thermal velocity is high. A medium with elevated plasma temperature can exhibit a significantly reduced total dE/dx over that of a cold target due to the substitution of the high stopping power of the bound electrons by the smaller cross-section of the free electrons. This has important consequences for neutron production efficiency.

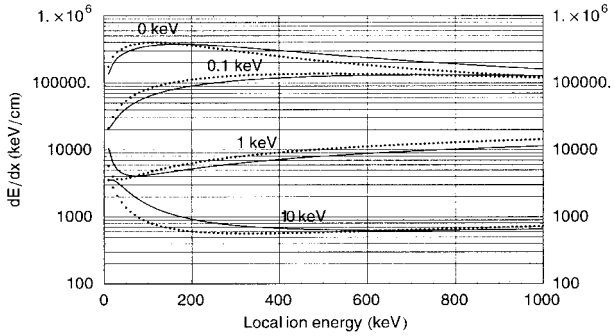

Figure 4. Stopping power dE/dx, for tritons slowing down in a solid density deuterium substrate (solid curves) and deuterons in a solid density tritium substrate (dotted curves), as a function of the ion energy. The electron temperature of the substrate is shown as a parameter.

Figure 4 shows the application of Eq. (8) to this case where the stopping powers for tritons slowing down on a solid density deuterium substrate (solid curves) are shown as a function of the ion energy, with the plasma temperature of the substrate as a parameter. Deuterons slowing down on a solid density tritium substrate (dotted curve) are shown for reference. Figure 5 shows the ion range resulting from our 1-D slab model. Note that at a target temperature of $T \sim 1$ keV, dE/dx is lowered by one to two orders of magnitude relative to a cold target ($T = 0$) with a commensurate increase in range.

Armed with this dE/dx formalism we can evaluate Eq. (7) to compute the neutron production efficiency. This is shown in Fig. 6 where the neutron yield per incident ion (i.e. with the fast ion current J in Eq. (7) set to unity) is plotted as a function of the initial mean kinetic energy $\bar{E}_0$ of the ion beam incident on the substrate for a range of substrate temperatures.

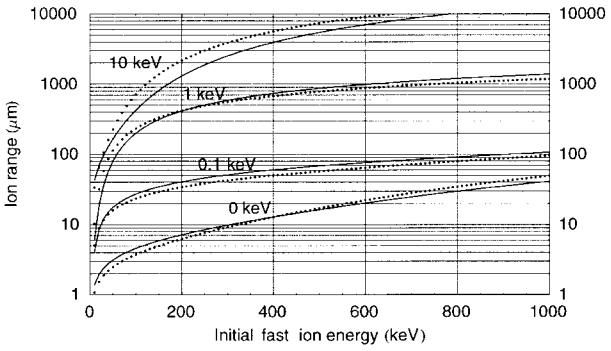

Figure 5. Resulting ion ranges for the stopping powers shown in Fig. 4. The solid curves show the triton range in a solid density deuterium substrate while the dotted curves show the converse, and are plotted as a function of the initial ion energy. The electron temperature of the substrate is shown as a parameter.

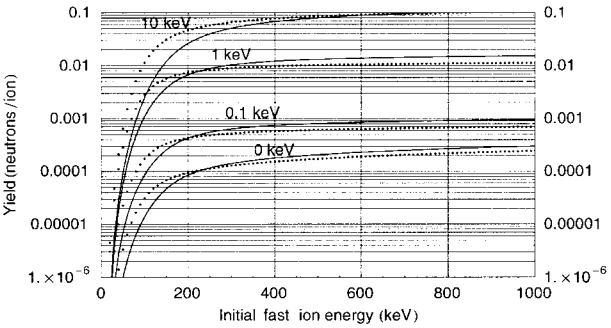

Figure 6. 14 MeV DT neutron production efficiency per incident ion for tritons interacting in a solid density deuterium substrate (solid curves) and deuterons interacting in a solid density tritium substrate (dotted curves) as a function of the initial ion energy. The electron temperature of the substrate is shown as a parameter.

The DT fusion cross-sections were taken from the latest evaluation by Bosch and Hale [35]. As these are thick target yields, the neutron production efficiencies increase monotonically with initial ion energy, and a knee in the yield curve is seen to occur around the peak in the DT cross-section in the laboratory frame. Note the significant advantages of producing initial ion energies above ∼200 keV and realizing substrate temperatures in the vicinity of ∼0.1–1 keV.

To compute neutron fluxes and absolute efficiencies, consider a laser, energy E_l, with pulse duration τ, focal spot (FWHM) of d_l, wavelength λ, repetition rate r_l and irradiance $I\lambda^2 - E_l\lambda^2/(\pi d_l^2\tau/4)$ incident on the conical target shown in Fig. 2. Assuming an isotropic distribution of ions from the tritium frost layer, the fraction directed inwards towards the deuterium substrate is

$$f_{in} \approx 1 - \frac{0.5}{\sqrt{1+(2A_{cone})^2}} \tag{9}$$

where A_{cone} is the cone aspect ratio, i.e. the ratio of the height to the diameter of the base. In the limit of a flat surface (i.e. $A_{cone} = 0$), $f_{in} = 0.5$ as expected.

The absolute fast ion current into the substrate becomes

$$J(E_l, I\lambda^2) \approx \frac{E_l r_l (1-\eta_{scatt})\eta_{ion}(E_l, I\lambda^2) f_{in}}{\bar{E}_0(E_l, I\lambda^2)} \tag{10}$$

where η_{scatt} is the fraction of incident laser energy scattered from the front surface and η_{ion} is the conversion efficiency of absorbed laser light into fast ions of initial mean kinetic energy $\bar{E}_0$.

We obtain the fusion Q value, i.e. the DT fusion energy output for a given incident laser energy input as

$$Q_{DT} \approx \frac{Y(\bar{E}_0, T) \times 17.6 \text{ MeV}}{E_l r_l}. \tag{11}$$

The 14 MeV neutron flux at the front face of a material specimen is then

$$\phi_{DT} \approx \frac{Y(\bar{E}_0, T)}{4\pi L^2} \tag{12}$$

where L is taken as the distance from the midpoint of the ion slowing down range in the substrate, i.e. the midpoint of the neutron production region, to the front face of the specimen. This includes the carbon debris shield thickness t_d and clearance gaps t_c each side of the shield as

$$L(\bar{E}_0, T) = 0.5R(\bar{E}_0, T) + t_d(E_l, \bar{E}_0, T) + 2t_c$$

where the ion slowing down range is

$$R(\bar{E}_0, T) = \int_{\bar{E}_0}^{0} \frac{dE_{ion}}{dE/dx(E_{ion}, T)}.$$

We use a spherical model to determine the thickness t_d of the sacrificial debris shield as $t_d = 2x$, where x is the real root of

$$\frac{E_l(1-\eta_{scatt})}{4\pi x\left(R(\bar{E}_0, T) + t_c + \frac{x}{2}\right)^2} = H_v. \tag{13}$$

Here, $H_v = 9.54 \times 10^4$ J/cm^3 is the specific volumetric vaporization energy of woven carbon cloth and was obtained from a cohesive energy of carbon of 59.6 MJ/kg [39] and a density of ∼1.6 g/cm^3. The factor of two ensures residual integrity of the shield over the minimum vaporization limit, including a safety margin.

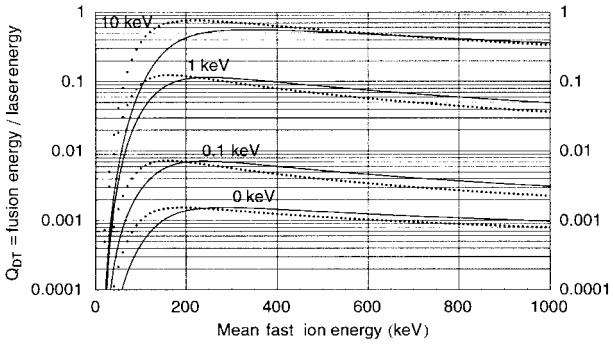

Figure 7. DT fusion Q values (i.e. DT fusion energy output divided by laser energy input) as a function of the initial mean fast ion energy $\bar{E}_0$ for a laser energy E_l = 100 J, and with $\eta_{scatt} = 30\%$ and $\eta_{ion} = 30\%$ assumed. The solid curves show tritons interacting in a solid density deuterium substrate while the dotted curves show deuterons interacting in a solid density tritium substrate. The electron temperature of the substrate is shown as a parameter.

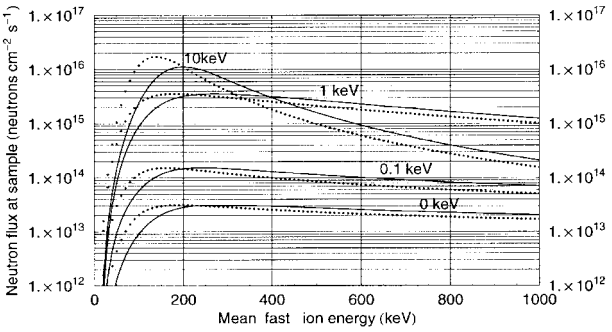

Figure 8. 14 MeV DT neutron flux at the front face of the specimen as a function of the initial mean fast ion energy $\bar{E}_0$ for a laser energy E_l = 100 J with repetition rate r_l = 100 Hz (average power of 10 kW) and with $\eta_{scatt} = 30\%$ and $\eta_{ion} = 30\%$ assumed. The solid curves show tritons interacting in a solid density deuterium substrate while the dotted curves show deuterons interacting in a solid density tritium substrate. The electron temperature of the substrate is shown as a parameter. Target–sample stand-off distances are a function of ion range and thus of $\bar{E}_0$ and are discussed in the text.

To parameterize the results for our system, we take a laser, energy E_l = 100 J with repetition rate r_l = 100 Hz (average power of 10 kW) and $\lambda = 1$ μm. We take clearance gaps of $t_c \sim 100$ μm each side of the debris shield. We assume a conical target of the type shown in Fig. 3 with an aspect ratio of $A_{cone} = 2$. Figure 7 shows the fusion Q value attainable (DT fusion energy output divided by laser energy input) as a function of the initial fast ion energy $\bar{E}_0$ with the substrate temperature T as a parameter and assumptions of $\eta_{scatt} = 30\%$ and $\eta_{ion} = 30\%$; i.e. a net conversion efficiency of incident laser energy into fast ions of 21%. Note, from Fig. 6, that Q values tend to maximize for initial ion energies of ∼150–250 keV for deuterons incident on a tritium substrate and ∼250–350 keV for the converse. These trends are discussed further in Section 7 where we perform self-consistent calculations of substrate temperatures.

Figure 8 shows the corresponding primary, uncollided 14 MeV neutron flux at the front face of a specimen with source specimen stand-off distances determined by Eq. (13) above. These are cycle averaged fluxes in n cm^{-2} s^{-1}, i.e. neutrons cm^{-2} pulse^{-1} times the laser repetition rate. Note that if a target temperature in the range ∼100–1000 eV could be sustained then neutron fluxes in the range 10^{14}–10^{15} n cm^{-2} s^{-1} may be achievable. Note also that at high initial ion energies and high target temperatures, the flux at the specimen actually drops. This is due to the long slowing down range of such high energy ions in the high temperature substrate, see the ion ranges in Fig. 5, which significantly increases the source–specimen distance L and decreases the neutron flux as $\sim 1/L^2$. Consequently, the optimum initial mean ion energies and target temperatures appear to be in the ranges ∼200–400 keV and ∼100–1000 eV, respectively. We note later that these fluxes depend on the feasibility of closed coupled target–specimen stand-offs of ∼0.1–0.2 cm and running clearances of ∼100 μm.

In Section 7 we provide a self-consistent case for fast ion production, substrate temperature and the resulting neutron production as a function of laser conditions.

6. Analysis for target option 3: exploding pusher target

Here, we consider the operation of option 3 targets (Fig. 2). These comprise DT micro-spheres of radius several tens of micrometres encased in a thin glass shell of a few micrometres thickness. Hot electrons generated by the high intensity laser absorbing on the outside of the shell penetrate the entire target and heat the glass shell rapidly to >2 keV, exploding it with several gigabar pressure and driving an inward shock of $\geq 5 \times 10^7$ cm/s. The centre of

mass of the shell or 'pusher' is almost stationary as it explodes both inward and outward. Since the DT fuel is preheated, it is on a high isentrope, so the fuel radius converges by only a factor of three or so [40]. The convergent shock heats the DT core to ∼10 keV.

Such electron conduction driven exploding pusher targets were the most common types of target utilized in the early stages of the ICF programme and were the first type to produce thermonuclear neutrons [40]. They can more easily achieve higher implosion velocities than conventional hot spot targets and, due to their low convergences, are tolerant of asymmetries in the drive. However, they do not scale to high gain because all the target mass is on a high isentrope, which precludes high compression.

We employed the LASNEX radiation–hydrodynamic code [41] to find optimal targets with the following fixed assumptions: a laser energy of 1 kJ at a wavelength of 1.06 μm symmetrically illuminates the glass DT filled micro-spheres. A fixed fraction of 20% of that energy is assumed to be absorbed, and the energy is distributed into a 'hot electron' thermal distribution, whose temperature T_H is given by the formula

$$T_H \text{ (keV)} = 30.0(I\lambda^2)^{0.4}. \tag{14}$$

This formula is in reasonable agreement with data from short pulse, high intensity laser–plasma interaction experiments and with Eqs (1) and (4) from Section 4. Here the laser intensity I is in units of 10^{17} W/cm^2 and the wavelength λ is in units of 1.06 μm light. The hot electrons then transport their energy throughout the target (chiefly heating the dense glass shell) as well as driving the expansion of the outer part of the target.

In the optimization search, we varied the pulse length of the laser, the radius of the shell, the thickness of the shell and the fill density of the DT fuel. The quantity T_H varied as we changed the pulse length or shell radius, since at fixed energy the intensity I varies inversely with the pulse length and R^2. In general the optimization procedure converged rapidly, by following the scaling arguments presented in Rosen and Nuckolls [42].

Yields in excess of 10^{12} neutrons per shot were produced by several combinations of parameters: for example, a 60 μm radius, 3 μm thick shell illuminated by a 15 ps FWHM Gaussian pulse and filled with 0.025 g/cm^3 DT gas, converged a factor of 3 from the initial fuel pusher radius to the minimum fuel pusher radius. As another example, a 45 μm radius, 4.5 μm thick shell illuminated by a 15 ps FWHM Gaussian pulse and filled with 0.05 g/cm^3 DT gas also exceeded 10^{12} neutrons. In both examples the peak ion temperatures exceeded 10 keV. Thus, a 10 Hz driver would supply ∼10^{14} n cm^{-2} s^{-1} at a sample 1 mm away from these targets.

We have also performed 1-D studies for targets that could be illuminated by a petawatt class facility at lower total energy. Here, we held fixed a 400 J laser source. An optimization study, otherwise identical to that described above, found target parameters that yielded 10^{11} neutrons/shot, more than adequate for good detection statistics. For example a 30 μm radius, 3 μm thick shell illuminated by a 7.5 ps FWHM Gaussian pulse and filled with 0.05 g/cm^3 DT gas achieved such a yield, with a convergence factor slightly larger than 3. Clearly, experiments may be within reach on present or near term facilities that can assess the predictions and, in particular, explore the cost trade-offs of illumination asymmetry performance.

We note that LASNEX simulations have also been performed by Callahan-Miller [43] on heavy ion driven, exploding pusher targets. She obtained yields of ∼5×10^{13} neutrons/pulse from the deposition of 5 kJ of heavy ions in ∼35 ps into a 10 μm gold shell surrounding a 35 μm radius cryogenic DT core. This represented a fusion gain $Q \sim 0.3\%$.

All of the above exploding pusher results were from 1-D simulations. Unlike conventional ICF targets, exploding pusher capsules do not require high compression ratios nor the creation of a central ignition hot spot. They are, therefore, tolerant of asymmetries in the drive and do not require high illumination symmetry. However, the effect of 2-D and 3-D asymmetries on capsule performance clearly needs to be addressed. Trade-offs between the performance of one and two sided illumination versus the requisite expense of two sided illumination driver schemes cannot be answered without such analyses. In the schematic diagram of Fig. 2, we show only single sided illumination of the capsule. Adequate performance under 2-D modelling may require two sided illumination but not uniform illumination over 4π. Such 2-D and 3-D analyses may also highlight deficiencies in the above clean 1-D yields.

7. 1-D target analysis

In this section, we extend the 1-D slab model from Section 5 to model fast ion production, slowing down, substrate temperature rise and substrate hydromotion, to obtain an approximately self-consistent case

Table 2. Target parameters from the 1-D model as a function of laser irradiance, $I\lambda^2$, for laser specifications of 100 J/pulse, 100 Hz repetition rate and a focal spot diameter (FWHM) of 50 μm. The pulse duration is determined by the irradiance requirement.

	Laser irradiance $I\lambda^2$ (W μm^2/cm^2)				
	10^{15}	10^{16}	10^{17}	10^{18}	10^{19}
Laser power (W)	1.79×10^{10}	1.79×10^{11}	1.79×10^{12}	1.79×10^{13}	1.79×10^{14}
Required pulse duration[a] (s)	5.58×10^{-9}	5.58×10^{-10}	5.58×10^{-11}	5.58×10^{-12}	5.58×10^{-13}
Hot electron temperature of T_2 frost layer (keV)	7.43	20.7	57.5	160	445
Mean fast ion energy $\bar{E}_0$ (keV)	25.2	70.0	195	542	1510
Fast ion range in D_2 substrate (cm) (= optimum substrate thickness)	0.00141	0.00802	0.0175	0.0257	0.0343
Mean substrate temperature T (keV)	0.158	0.454	0.409	0.317	0.236
Average neutron yield at 100 Hz (neutrons s^{-1})	1.86×10^{11}	2.32×10^{13}	1.38×10^{14}	7.13×10^{13}	2.11×10^{13}
Yield/shot (neutrons per shot)	1.9×10^{9}	2.3×10^{11}	1.4×10^{12}	7.1×10^{11}	2.1×10^{11}
Fusion Q value	5.3×10^{-5}	0.0066	0.039	0.020	0.0059
14 MeV neutron flux at sample (cm^{-2} s^{-1})[b]	1.08×10^{12}	1.45×10^{14}	9.47×10^{14}	5.27×10^{14}	1.66×10^{14}

[a] Determined by required laser irradiance ($I\lambda^2$) at fixed energy and focal spot size.
[b] Measured at the front face of specimen; mid-specimen fluxes would be little different due to their small size (~0.1–1 mm).

for neutron production as a function of the laser intensity for the target design of option 1.

We operate in the medium irradiance regime (i.e. $I\lambda^2 \leq 10^{18}$ W μm^2/cm^2) with a target design of the form shown in Fig. 3. Here, laser energy is initially absorbed by the electrons via collisional absorption followed by subsequent transfer to fast ions which are responsible for heating the target substrate material. Thus, determination of the ion dE/dx and resulting range in the substrate requires the determination of the coupled, time dependent substrate temperature T according to

$$\frac{d}{dt}(3nkT) \approx \frac{E_l \eta_{ion}(1-\eta_{scatt})}{V_{subst}(T,\bar{E}_0)\tau_{eff}(T,\bar{E}_0)} - \frac{3nkT}{\tau_E(T,\bar{E}_0)} - P_{rad}(T). \quad (15)$$

The first term on the RHS is the power deposited per unit volume in the substrate due to fast ions. Here, $V_{subst}(T,\bar{E}_0)$ is the heated substrate volume and is a function of substrate temperature T (one fluid model) and the initial mean fast ion kinetic energy $\bar{E}_0$ through the ion slowing down range. The effective time constant for ion heating of the substrate is taken as $\tau_{eff}(T,\bar{E}_0) \approx \sqrt{\tau^2 + \tau_{ion}^2}$, and is determined by the longer of the laser pulse length, τ, and the time for ions to be accelerated across the sheath and slow down in the substrate, τ_{ion}. The second term on the RHS of Eq. (15) is the rate of thermal energy loss. As each side of the substrate is a vacuum boundary, we neglect electron heat conduction and take $\tau_E(T,\bar{E}_0) \sim R(T,\bar{E}_0)/c_s(T)$, where $R(T,\bar{E}_0)$ is the substrate thickness set equal to the ion slowing down range and $c_s(T)$ is the sound speed for substrate disassembly. The ion slowing down and subsequent electron heating of the substrate occurs in the 10–10 ps time frame, i.e. much shorter than the thermal disassembly time of the substrate. Thus the substrate flashes to a solid plasma of tens to hundreds of eV. The third term on the RHS of Eq. (15) is radiation loss via bremsstrahlung, which scales as $\sim T^{1/2}$.

Table 2 shows the results of applying Eq. (15) to the target design of Fig. 3 for the following laser conditions: energy/pulse $E_l = 100$ J, repetition rate $r_l = 100$ Hz (average power of 10 kW), $\lambda = 1$ μm, a focal spot size (FWHM) of $d_l = 50$ μm, and where the laser irradiance $I\lambda^2$ is varied from 10^{15} to 10^{19} W μm^2/cm^2 by adjusting the pulse length τ from 3.18×10^{-8} to 3.18×10^{-12} s, respectively. The focal spot diameter of 50 μm is determined by a target stand-off distance of 1 m from the final focusing

optic, and the assumption of a 2.5 times diffraction limited beam. At each irradiance, we apply Gitomer's empirical scaling from Eq. (1) to obtain the initial hot electron temperature of the tritium frost layer and then deduce the mean energy of the expelled fast ions $\bar{E}_0$ by the sheath potential through which they are accelerated as expressed by Eq. (2). As the literature does not yet reveal consistent scalings for the efficiency of fast ion production versus $I\lambda^2$, we take $\eta_{scatt} = 30\%$ and $\eta_{ion} = 30\%$ as in Section 5. From Eq. (15), we then solve for the resulting target temperature and optimum substrate thickness, where the latter is determined by the ion slowing down range $R(T, \bar{E}_0)$. Finally, from the formalisms of Eq. (7) through (13), we compute the resulting neutron yield, the required carbon debris shield thickness, the stand-off distance from the target to the material test specimen, and the neutron flux at the front face of the latter.

We see from Table 2 that the mean fast ion energies range from ∼25 keV at $I\lambda^2 = 10^{15}$ W μm^2/cm^2 to ∼1.5 MeV at $I\lambda^2 = 10^{19}$ W μm^2/cm^2. Across this range, the substrate temperatures are several hundred eV and the range is only a weak function of irradiance because the increased heating rate is balanced by a longer ion range and thus a larger volume for power deposition. Below ∼10^{15} W μm^2/cm^2, however, the substrate temperature will fall rapidly.

Also from Table 2 we note an optimum in the fusion Q and the neutron flux at the specimen around $I\lambda^2 \sim 10^{17}$–10^{18} W μm^2/cm^2, a result of three factors:

(a) Increasing mean fast ion energy with increasing $I\lambda^2$ results in fewer fast ions in total for the fixed laser energy of 100 J/pulse and fixed η_{ion},

(b) Higher mean fast ion energies give diminishing returns relative to the peak of the DT cross-section at 160 keV,

(c) Higher mean fast ion energies have longer ion ranges in the substrate thus requiring greater substrate thicknesses and greater stand-off distances to the sample.

Thus, given this model, irradiances of $I\lambda_2 \sim 10^{17}$ appear to be optimum to maximize the 14 MeV neutron flux at the front face of the specimen at around 10^{15} cm^{-2} s^{-1} for this target type. However, we make the following caveats:

(i) Our thin target, space charged limited model for fast ion acceleration may not be applicable at $I\lambda^2 \geq 10^{18}$ where the hot electrons become relativistic and direct fast ion production becomes efficient (Section 4). An option here perhaps is to switch to a single region DT target as in option 2.

(ii) A constant fast ion production efficiency of $\eta_{ion} \sim 0.3$ is assumed [11, 12, 15, 19, 24–26] although, in reality, this is a complex function of $I\lambda^2$ and target conditions. Quantitative experiments are required to determine predictive behaviour.

(iii) The neutron fluxes in Table 2 are computed at the front face of the specimens. Due to the small size of the samples (∼100–1000 μm), the mid-specimen fluxes would not decrease appreciably. However, the numbers in Table 2 also assume the attainment of closed coupled specimens with target–specimen stand-off distances of ∼0.2 cm. Should larger clearances of, say, 0.5 cm, be required in a fully practical system, these fluxes will be reduced by a factor of ∼10.

The capital cost of a full irradiation facility based on the results of Table 2 for a 10 kW average power laser system, might be in the range ≤US M$100. This preliminary estimate is based on a laser and target facilities cost obtained by scaling with power from the present 'Mercury' diode pumped, solid state experimental facility at LLNL [44]. Also, we assume ∼US M$50 for conventional facilities including shielded experimental areas, hot cells and buildings per the conceptual design of the International Fusion Materials Irradiation Facility [10].

8. Applications to fusion material research

Capabilities for multiscale, predictive modelling of radiation induced microstructure and mechanical property changes in irradiated materials are reaching a high degree of sophistication. Physically based modelling and simulation tools can be coupled across all relevant length and time scales [45]. Of course, such models require stringent validation in order to become fully viable predictive tools. The 14 MeV neutron source concepts proposed here offer the potential to irradiate materials at different temperatures, fluxes and pulse rates. When coupled with advanced, post-irradiation assay techniques, such results could play an important role in the development and validation of such multiscale modelling tools which can then be applied to predict the extrapolated behaviour of full size, engineering scale fusion materials.

At the shortest timescale, molecular dynamics (MD) simulations on ASCII class massively

parallel computers can describe the form of the primary damage state [46–58], i.e. the number and state of clustering of the produced defects as a function of recoil energy. To link the timescales, kinetic Monte Carlo (KMC) methods are used to determine how the produced defects are able to escape their nascent cascade and migrate through the lattice to produce microstructural and microchemical changes [46, 49–53]. These linked MD–KMC simulations can be carried out at doses and dose rates identical to those used in a given set of irradiation experiments. Their output is the spatial and temporal distribution of defects, impurity atoms, voids, impurity precipitates and sink (dislocation) microstructure.

Our post-irradiated microspecimens would be used to comprehensively validate these models using the assay techniques of micromechanical testing, transmission electron microscopy, synchrotron based X ray diffraction, etc. [45]. Then, employing 3-D dislocation dynamics simulation codes [54–58], these data would be used to predict how these microstructure features alter the mechanical properties of bulk irradiated material. Such simulations provide a complete description of the plastic behaviour of a single grain of material and of the microstructure development under an applied load, including the locking and immobilization of dislocation by irradiation induced loops and precipitates. Moreover, the simulations provide a prediction of the stress–strain curve for a given starting microstructure and thus a prediction of the yield stress and the strain hardening exponents as a function of irradiation dose. Finally, the constitutive relations obtained from these fundamental studies can then be used to provide predictive strength models for polycrystalline materials (e.g. vanadium alloys) or composites (e.g. C–C and SiC–SiC) for use in continuum computer code simulations including full 3-D finite element codes. Therefore, the small dimensions of the irradiated specimens ($\sim$100–1000 μm) envisaged for use here do not present any fundamental limitation in our ability to characterize large irradiated volumes of single materials. Of course, our small volume samples cannot generate composite data on the behaviour of large scale, engineering structures, for example, a welded blanket module comprising a number of heterogeneous materials and coolants. This will have to await the construction of an engineering test reactor of appreciable fusion power (>100 MW) and costs in the multi-billion dollar range. Accordingly, a cost effective, high yield laser neutron source can be viewed as a near term complementary facility to provide a comprehensive predictive database for polycrystalline and composite structural materials.

In future ICF power plants, the response of structural materials to the pulsed nature of neutron irradiation may be different to that sustained under steady state continuous irradiation [58, 59]. The main reason for this is that the vacancy mean lifetime can be shorter than $\sim$0.1 s at elevated temperatures, thus enhancing the annealing kinetics of the microstructure. Under some conditions the materials response at the same dose and temperature is enhanced, while it is reduced under other conditions, as compared with steady state irradiation. Differences have been demonstrated for irradiation swelling [60–62], irradiation creep [63, 64], point defect production [57] and irradiation hardening [62]. Under intense pulsed irradiation, the temporal rate of damage production is significantly increased, leading to well known rate effects on the response of materials. Clustering of point defects is enhanced, and point defect recombination is also increased. This is a direct result of such reactions being of a non-linear nature, similar to second order chemical reactions. Accordingly, the micro neutron source presented in this article might also prove a useful experimental facility to explore these basic aspects of pulsed irradiation for applications in ICF systems if laser repetition rates are kept below a few hertz. On the other hand, if the pulsing frequency is greater than a few tens of hertz, it is expected that the response of the material will approach that of steady fusion irradiation. Thus, by adjusting the pulse repetition rate, the facility could, in principle, be tailored to give materials damage information for both ICF and magnetically confined fusion systems.

9. Recommendations for further research

We have shown the potential for using fast pulse, high intensity lasers to produce 14 MeV DT neutron fluxes of around 10^{15} n cm^{-2} s^{-2} at fusion material test specimens of dimensions $\sim$0.1–1 mm. Because of the small target volumes and the removal of input driver heat by sacrificial vaporization, such laser driven plasma targets are potentially able to produce high neutron fluxes at modest cost relative to conventional beam–target neutron sources with cold (i.e. solid or liquid) substrates. Principal issues requiring further R&D include:

(a) Quantitative experimental data on the interaction of fast pulse, high intensity lasers with targets, particularly the mechanisms for high efficiency fast ion production;

(b) PIC simulations and experiments with candidate targets to project neutron yields and fusion gains attainable with affordable laser energies of ∼100 J to ∼1 kJ, repetition rates of ∼10–100 Hz, and average power levels of ≤10 kW;

(c) Engineering designs of practical laser–target systems for the stand-off and protection of close coupled micromaterials specimens;

(d) A materials science/computational effort to couple the evaluation of post-irradiation, microspecimen assays to multiscale, predictive modelling codes.

Acknowledgements

The authors take pleasure in acknowledging informative discussions with M. Key, G. Guethlein, E.M. Campbell, P. Rambo, T.C. Sangster, H. Powell, C. Bibeau, W. Wolfer and K. Estabrook of Lawrence Livermore National Laboratory, R. Stoller, A. Rowcliffe, E. Bloom and S. Zinkle of Oak Ridge National Laboratory, and T. Mehlhorn of Sandia National Laboratory.

This work was performed under the auspices of the US Department of Energy by Lawrence Livermore National Laboratory under Contract Number W-7405-Eng-48.

References

[1] Perry, M.D., Mourou, G., Science **264** (1994) 917.
[2] Gibbon, P., Forster, E., Plasma Phys. Control. Fusion **38** (1996) 769.
[3] Abdou, M.A., et al., Nucl. Fusion **27** (1987) 619.
[4] Baker, C.C., et al., Technical Planning Activity — Final Report, Rep. ANL/FPP-87-1, Argonne National Lab., IL (1987) Ch. 5.
[5] Kessler, G., Cacuci, D., Cierjacks, S. (Eds), Nucl. Sci. Eng. **106** (1990) 99.
[6] Petzoldt, R.W., Moir, R.W., Fusion Technol. **30** (1996) 73.
[7] Doran, D.G., et al., Evaluation Committee on the Los Alamos Spallation Radiation Effects Facility: Final Report, Rep. PNL-SA-18584, Battelle Pacific Northwest Lab., Richland, WA (1990).
[8] Harkness, S.D., et al., Fusion Energy Advisory Committee Panel Report on the Fusion Materials Research Program, US Department of Energy, Washington DC (1998).
[9] Heikkinen, D.W., Logan, C.M., Davis, J.C., Nucl. Sci. Eng. **106** (1990) 228.
[10] Shannon, T.E., et al., "Conceptual design of the International Fusion Materials Irradiation Facility (IFMIF)", J. Nucl. Mater. (in press).
[11] Lisowski, P.W., et al., Nucl. Sci. Eng. **106** (1990) 208.
[12] Coensgen, F.H., et al., Nucl. Sci. Eng. **106** (1990) 138.
[13] Peng, M.Y.-K., et al., J. Fusion Energy **17** (1998) 45.
[14] Ruytov, D.D., Plasma Phys. Control. Fusion **32** (1990) 999.
[15] Bloom, E., Wiffen, W. (Eds), Fusion Materials Semi-Annual Progress Report for Period Ending Dec. 31, 1998, US Department of Energy Rep. DOE/ER-0313/25, USDOE, Washington, DC (1999).
[16] Ditmire, T., et al., Nature **386** (1997) 54.
[17] Ditmire, T., et al., Phys. Rev. Lett. **78** (1997) 3121.
[18] Kruer, W.L., The Physics of Laser Plasma Interactions, Addison-Wesley, Reading, MA (1988).
[19] Forslund, D.W., Phys. Rev. Lett. **48** (1982) 1614.
[20] Gitomer, S.J., et al., Phys. Fluids **29** (1986) 2679.
[21] Gross, R.A., Fusion Energy, Wiley, New York (1984) 132.
[22] Kruer, W.L., Estabrook, K.G., Phys. Fluids **20** (1977) 1688.
[23] Estabrook, K.G., Kruer, W.L., Phys. Rev. Lett. **40** (1978) 42.
[24] Manes, K.R., et al., J. Opt. Soc. Am. **67** (1977) 717.
[25] Kruer, W.L., The Physics of Laser Plasma Interactions, Addison-Wesley, Reading, MA (1988) 159.
[26] Fews, A.P., et al., Phys. Rev. Lett. **73** (1994) 1801.
[27] Wilks, S.C., et al., Phys. Rev. Lett. **69** (1992) 1383.
[28] Meyerhofer, D.D., et al., Phys. Fluids B **5** (1993) 2584.
[29] Guethlein, G., Lawrence Livermore Natl Lab., CA, personal communication, 1998.
[30] Pretzler, G., et al., Phys. Rev. E **58** (1998) 1165.
[31] Norres, P.A., et al., Plasma Phys. Control. Fusion **40** (1998) 175.
[32] Denavit, J., Phys. Rev. Lett. **69** (1992) 3052.
[33] Lawson, W.S., et al., Phys. Plasmas **4** (1997) 788.
[34] Perry, M.D., Lawrence Livermore Natl Lab., CA, personal communication, 1998.
[35] Bosch, H.S., Hale, G.M., Nucl. Fusion **32** (1992) 611.
[36] Mehlhorn, T.A., J. Appl. Phys. **52** (1981) 6522.
[37] Jackson, J.D., Classical Electrodynamics, Wiley, New York (1975) 618ff.
[38] Linhard, J., et al., Mat. Phys. Medd. **33** (1963) 14.
[39] Chemical Rubber Company, Handbook of Chemistry and Physics, 55th edn, CRC Press, Boca Raton, FL (1974).

[40] Lindl, J., Inertial Confinement Fusion, AIP and Springer-Verlag, New York (1998).
[41] Zimmerman, G.B., Kruer, W.L., Comments Plasma Phys. **2** (1975) 51.
[42] Rosen, M.D., Nuckolls, J.H., Phys. Fluids **22** (1979) 1393.
[43] Callahan-Miller, D., Lawrence Livermore Natl Lab., CA, personal communication, 1998.
[44] Marshall, C., et al., in Optical Society of America Trends in Optics and Photonics, Vol. 19 (Bosenberg, W., Fejer, M., Eds), Optical Society of America, Washington, DC (1998).
[45] Bulatov, V., Diaz de la Rubia, T. (Eds), "Multiscale Modeling of Materials", Proc. Symp. Mater. Res. Soc. **538** (1999).
[46] Diaz de la Rubia, T., Ann. Rev. Mater. Sci. **26** (1996) 613.
[47] Averback, R.S., Diaz de la Rubia, T., Solid State Phys. **51** (1998) 281.
[48] Bacon, D.J., et al., J. Nucl. Mater. **251** (1997) 1.
[49] Heinisch, H.L., Nucl. Instrum. Methods Phys. Res. B **102** (1995) 47.
[50] Heinisch, H.L., Singh, B.N., J. Nucl. Mater. **251** (1997) 77.
[51] Soneda, N., Diaz de la Rubia, T., Phil. Mag. A (in press).
[52] Diaz de la Rubia, T., et al., J. Nucl. Mater. **251** (1997) 13.
[53] Ghoniem, N.M., J. Nucl. Mater. **179** (1991) 99.
[54] Kubin, L.P., Canova, G., Scr. Metall. **27** (1993) 957.
[55] Kubin, L.P., Treatise in Materials Science and Technology (Cahn, R.W., et al., Eds), VCH, Weinhum (1993).
[56] Rhee, M., et al., Model. Sim. in Mater. Sci. Eng. (in press).
[57] Huang, H., et al., "Stability of dislocation short-range reactions in BCC crystals" (in preparation).
[58] Ghoniem, N.M., "Curved parametric segments for the stress field of 3-d dislocation loops" (in preparation).
[59] Ghoniem, N.M., Kulcinski, G.L., Nucl. Technol./ Fusion **2** (1982) 165.
[60] Simonen, E.P., Ghoniem, N.M., Packan, N.H., J. Nucl. Mater. **122&123** (1984) 391.
[61] Ghoniem, N.M., Kulcinski, G.L., J. Nucl. Mater. **85&86** (1979) 547.
[62] Ghoniem, N.M., J. Nucl. Mater. **89** (1980) 359.
[63] Gurol, H., Ghoniem, N.M., Wolfer, W.G., J. Nucl. Mater. **99** (1981) 1.
[64] Gurol, H., Ghoniem, N.M., Wolfer, W.G., J. Nucl. Mater. **103&104** (1981) 251.
[65] Sawan, M.E., Kulcinski, G.L., Ghoniem, N.M., J. Nucl. Mater. **103&104** (1981) 109.

(Manuscript received 17 February 1999
Final manuscript accepted 12 August 1999)

E-mail address of L.J. Perkins:
perkins3@llnl.gov

Subject classification: L0, It